

Electronic Supplementary Information

Destructive Quantum Interference in Heterocyclic Alkanes: The Search for Ultra-short Molecular Insulators

Boyuan Zhang,^{1†} Marc H. Garner,^{2†} Liang Li,³ Luis Campos,³ Gemma C. Solomon,^{2,*} and Latha Venkataraman^{1,3,*}

¹Department of Applied Physics and Applied Mathematics, Columbia University, New York, New York 10027, United States

²Nano-Science Center and Department of Chemistry, University of Copenhagen, Universitetsparken 5, 2100 Copenhagen Ø, Denmark

³Department of Chemistry, Columbia University, New York, New York 10027, United States

[†] equal contribution

Table of Contents

1. STM-Break Junction experiment details	S2
2. Additional Figures	S2
3. Conformational Analysis	S5
4. Computational Details	S8
6. References	S11

1. STM-Break Junction experiment details

Conductance measurements were made using a custom-built scanning tunneling microscope that has been described in detail before¹. Conductance measurements were performed in dilute solutions (100 μ M) of the molecules in 1,2,4-trichlorobenzene (TCB). One-dimensional (1D) conductance histograms are constructed using logarithmic bins (100/decade), and two-dimensional (2D) histograms use logarithmic bins along the conductance axis (100/decade) and linear bins (1000/nm) along the displacement axis. The junction length is determined by displacement profiling of the molecular conductance feature in the two-dimensional histograms.

2. Additional Figures

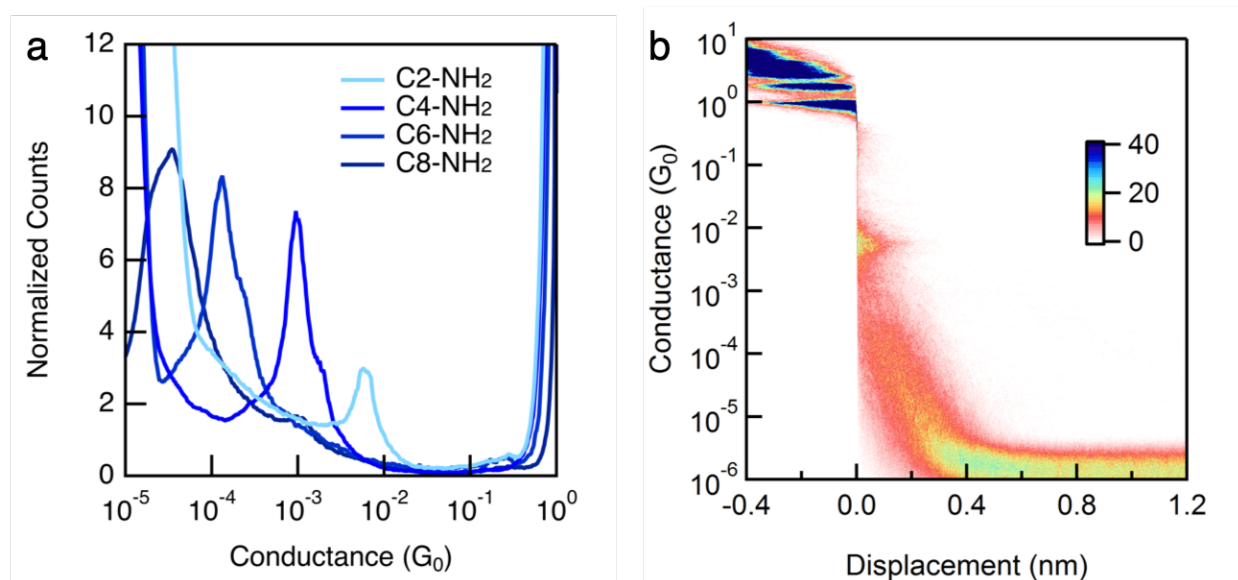


Figure S1. (a) Logarithm-binned 1D conductance histograms **C2-NH₂**, **C4-NH₂**, **C6-NH₂** and **C8-NH₂** measured in TCB compiled from thousands of traces without any data selection. Note that the increase in counts at low conductances for **C2-NH₂**, **C4-NH₂**, **C6-NH₂** is due to the noise floor as these measurements are done at 25 mV, 100 mV, 100 mV and 250 mV for **C2-NH₂**, **C4-NH₂**, **C6-NH₂**, **C8-NH₂**. (b) Logarithm-binned 2D conductance-displacement histograms of **C2-NH₂** measured in TCB at 100 mV.

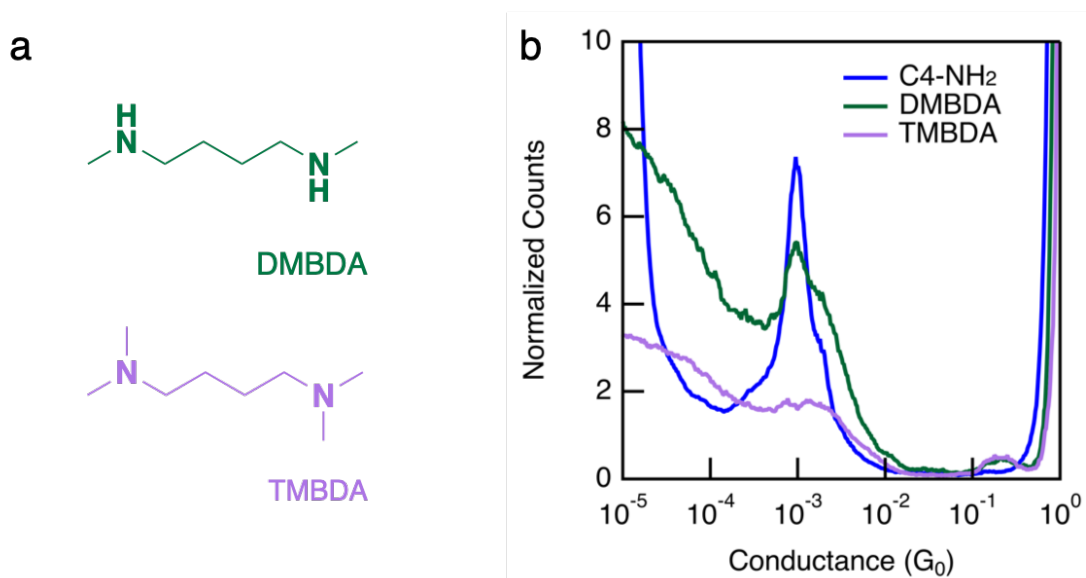


Figure S2. (a) Structure of N,N'-dimethyl-1,4-butanediamine (**DMBDA**) and N,N,N',N'-tetramethyl-1,4-butanediamine (**TMBDA**). (b) Logarithm-binned 1D conductance histogram of **TMBDA** and **DMBDA** along with the histogram of **C4-NH₂**.

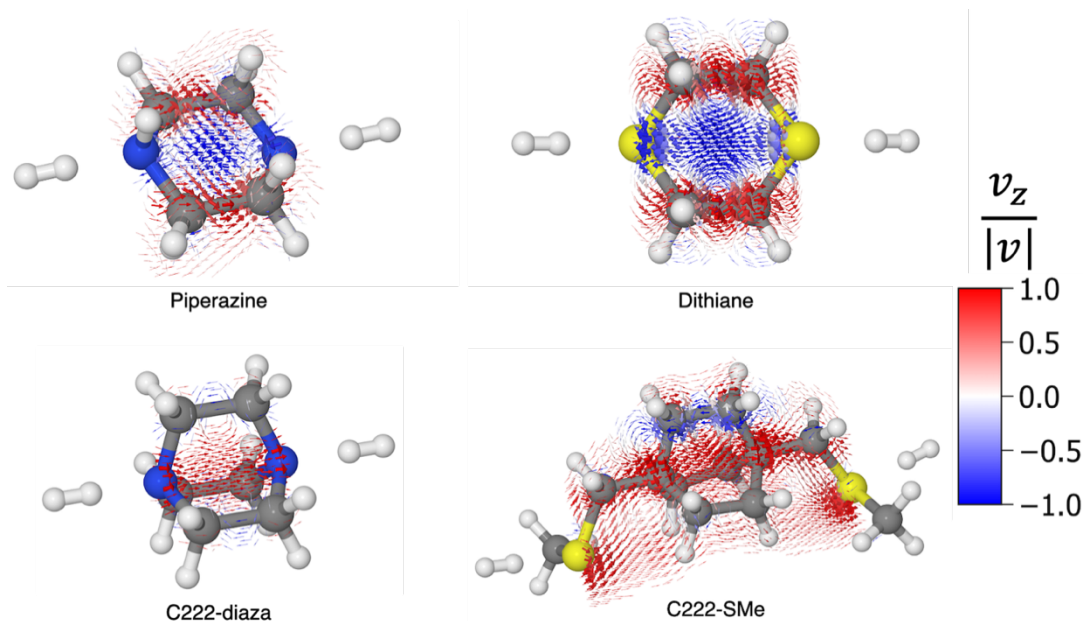


Figure S3. Ballistic current density calculated at the Fermi energy of **piperazine**, **dithiane**, **C222-diaza**, and **C222-SMe** calculated using wide-band approximated electrodes. The electrode positions are shown as dihydrogen molecules. Vectors are shown as arrows where the diameter is scaled by the vector length and colored by the relative magnitude of the z-component of the vector.

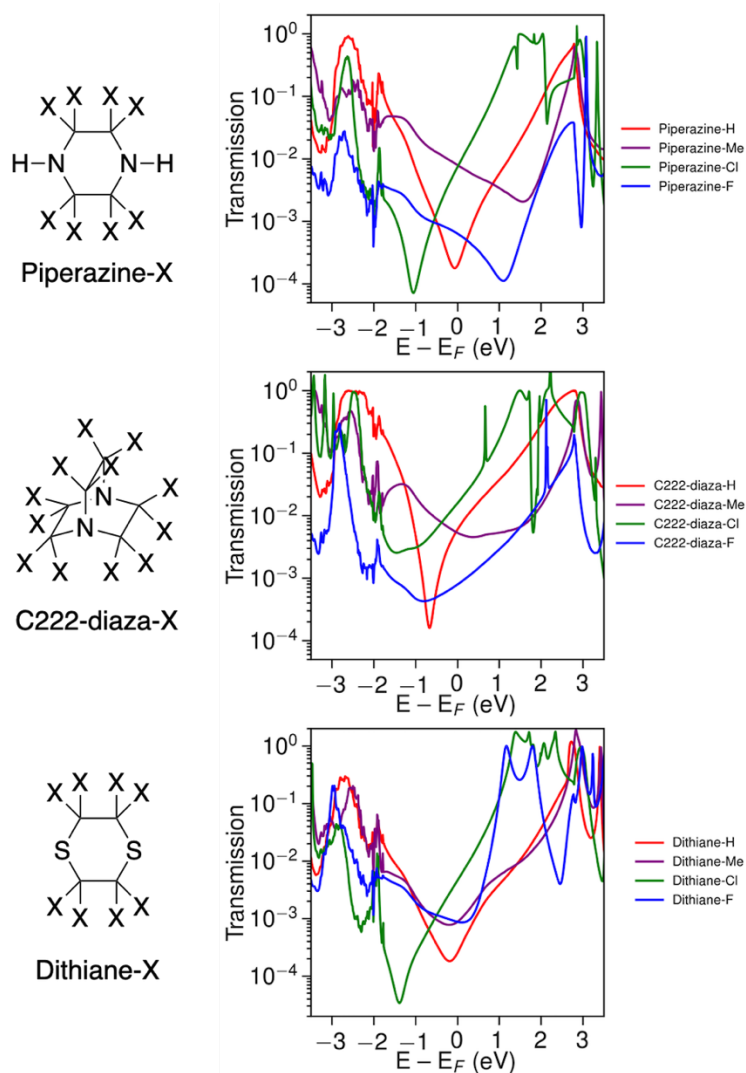


Figure S4. Au-molecule-Au junction transmission of substituted **piperazine**, **C222-diaza**, and **dithiane**. Transmission is calculated using Au-electrodes as described in the manuscript and part 4 below.

The model transmission matches that obtained with DFT very well. The sharp antiresonance structure for **piperazine** near E_F originates primarily from a destructive interference between the HOMO and LUMO which have the same phases ($\theta_{\text{HOMO}} - \theta_{\text{HOMO}-1} = 0$). This can be further confirmed by looking at the calculated MOs shown in Figure S5c. The HOMO and LUMO have same parity at the lone-pair of nitrogen which couples to the leads. For **dithiane**, the antiresonance originates primarily from a destructive interference between the HOMO and LUMO+1 which have the same phases ($\theta_{\text{HOMO}} - \theta_{\text{HOMO}-1} = 0$). The HOMO and LUMO+1 have same parity at the sulfur which couples to the leads. In the reconstructed transmission function, the LUMO is nearly 2 to 3 orders of magnitude less coupled to the leads than the other MOs; therefore, resulting into the very sharp resonance structure.

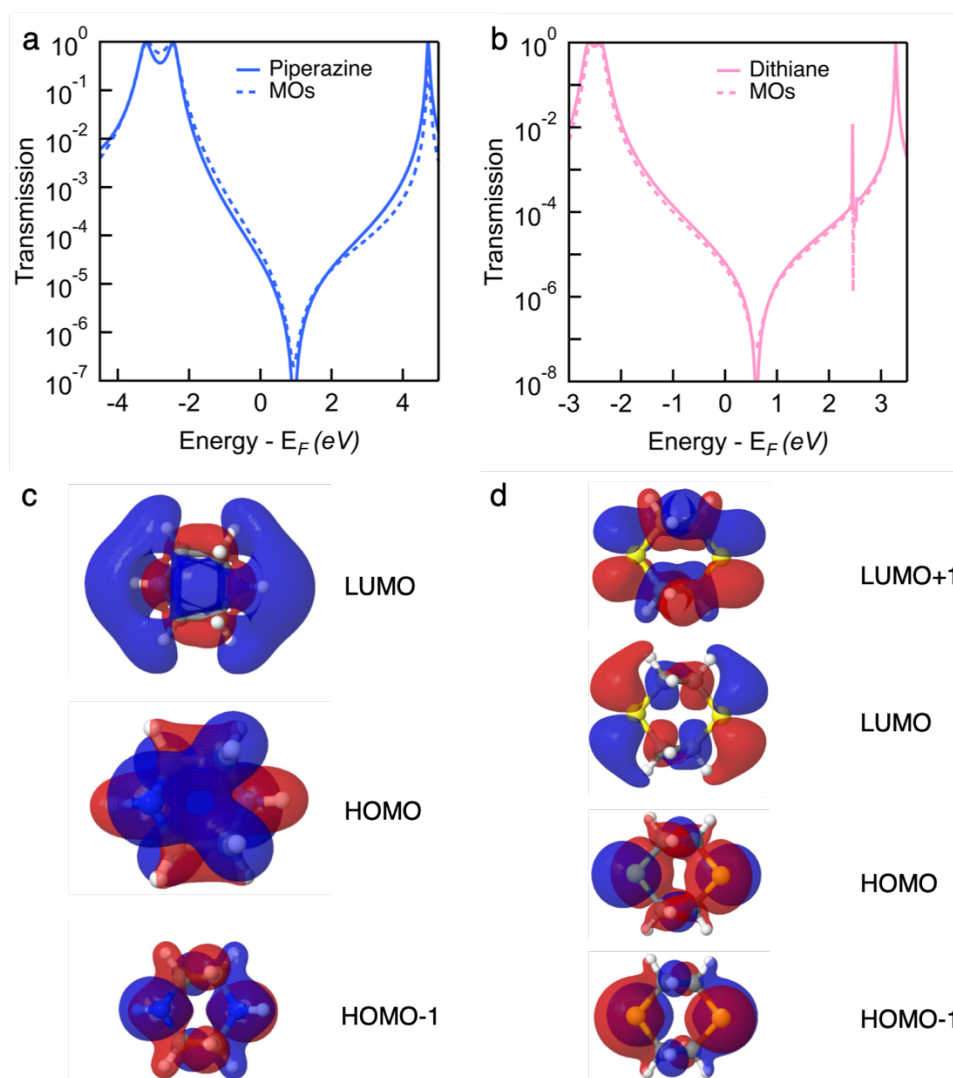


Figure S5. (a) Transmission functions of **piperazine**, calculated as $T(E) = |t_{\text{LUMO}} + t_{\text{HOMO}} + t_{\text{HOMO-1}}|^2$ (solid line) overlaid with Landauer transmission in the wide-band limit (dashed). (b) Transmission functions of **dithiane**, calculated as $T(E) = |t_{\text{LUMO+1}} + t_{\text{LUMO}} + t_{\text{HOMO}} + t_{\text{HOMO-1}}|^2$ (solid line) overlaid with Landauer transmission in the wide-band limit (dashed). MOs of (c) **C222-diaza** and (d) **dithiane** calculated using DFT with B3LYP functional. White, black, blue and yellow atoms represent H, C, N and S, respectively.

3. Conformational Analysis

The molecules we study have different degrees of conformational freedom. **C222-diaza** has no conformational freedom as the cage is rigid. **C222-SMe** has limited conformational freedom in its methylthiomethyl linkers which was discussed in previous work;² here we include only the *anti*-conformation. **Piperazine** and **dithiane** both have conformational freedom due to their six-membered ring structures. We will discuss their conformations and their relevance when analyzing the conducting properties of the systems.

We compute the energies of optimized structures using DFT as implemented in Gaussian09 at the M06-2X(D3)/6-311G(d,p) level of theory.^{3,4} All structures were optimized using to the *verytight* criteria with integrals evaluated on *ultrafine* grid, and a frequency analysis was carried out to confirm the structures are local energy minima. All optimized structures are available online as xyz files. Au-molecule-Au junctions were optimized as described in the computational details section.

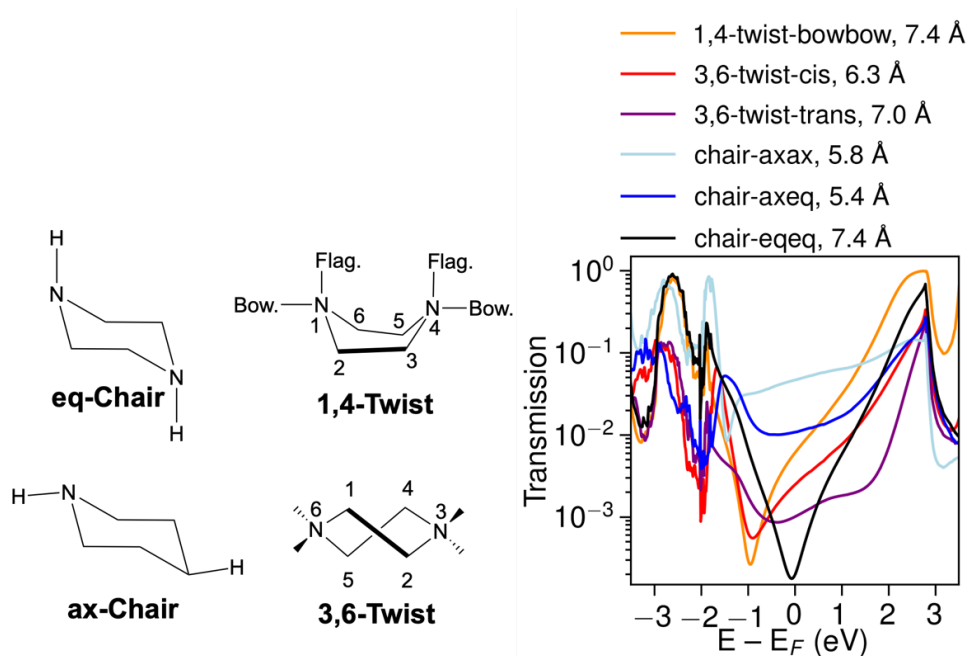


Figure S6. Overview of possible conformations of **piperazine**, and Au-molecule-Au junction transmission with Au-Au tip-to-tip length.

Piperazine has one chair and two possible twist-boat conformations, which are illustrated in Figure S6. Each of these have the possibility of having the nitrogen lone-pair in axial/flagpole or equatorial/bowsprit positions. The nitrogen lone-pair binds to the Au electrodes through dative bonding, and therefore we name the conformers after the orientation of the N lone-pair; the hydrogen atoms will be in the opposite position. For the chair conformation, there are two *trans*-conformations where both lone-pairs are in axial (axax) or equatorial (eqeq) orientation, and one *cis*-conformation where one lone-pair is in axial and one is in equatorial position (axeq). In similar fashion, there are three 1,4-twist conformations: flagflag, flagbow, and bowbow. In the 3,6-twist all four positions are equivalent and there are no axial/equatorial positions; there is thus only a *cis* and a *trans* conformer. All 8 combinations are found to be local energy minima and their zero-point corrected energies are listed in Table S1. As one might have expected based on the parent cyclohexane conformations, the chair conformers are the most stable, while all twist conformations are around 0.3 eV higher in energy. We therefore expect twist conformations to be negligible in the junction experiments. The chair conformations are energetically near-degenerate. However, in

junction experiments the molecule is being pulled, and the full extension length differs for the chair conformers due to the difference of axial and equatorial positions. Listed in Figure S6, the computed junction length of the chair-axax and chair-axeq are shorter than chair-eqeq. Considering the snapback of the electrodes in break-junction experiments, chair-axax and chair-axeq are likely to be too short to be measure in STM-BJ experiments. We cannot rule out that twist conformers appear in experiments, especially because a chair flip will normally occur through twist conformers.² Shown in Figure S6, the transmission of the twist conformers are similarly low with the chair-eqeq conformer, and these are unlikely to be distinguishable in experiment. We note that 1,4-twist conformers with one or both nitrogen lone-air in flagpole positions cannot easily form junctions as the lone-pair is not pointing along the transport direction. In our simulations these junction break during optimization, and considering their very short length and high energy, they are unlikely to form junctions.

Table S1. Energies of **piperazine** conformations optimized in vacuum (M06-2X(D3)/6-311G(d,p)).

Conformations (vacuum)	eV
14twist_flagflag	0.39
14twist_bowbow	0.29
14twist_flagbow	0.27
36twist_cis	0.34
36twist_trans	0.34
chair_axax	0.00
chair_axeq	0.02
chair_eqeq	0.05

Dithiane only has the three basic conformations in vacuum as there are no axial and equatorial substituents, as shown in Figure S6. The zero-point corrected energies are listed in Table S2. The chair conformation is the more stable than the 3,6-twist. We do not find the 1,4-twist to be a local energy minimum. In junctions the Au-electrodes will couple into one sulfur lone-pair on each end of the molecule, and there is thus similar junction conformations as in **piperazine**. Their transmission and simulated junction lengths are shown in Figure S6. Although, the axax and axeq chair conformations are short than the eqeq chair, all **dithiane** conformations are longer than those of **piperazine** because C-S and Au-S bond lengths are longer than the equivalent C-N and Au-N bond lengths. These shorter axial chair conformations have higher transmission, and may be responsible for the noisy higher conductance peaks observed in Figure 2c. These appear at short junction lengths during the pulling experiments as seen in Figure 2a, and we therefore attribute these to shorter chair conformations with one or both electrodes in an axial position. The 3,6-twist conformations are almost as long as the eqeq chair, and have similar low transmission.

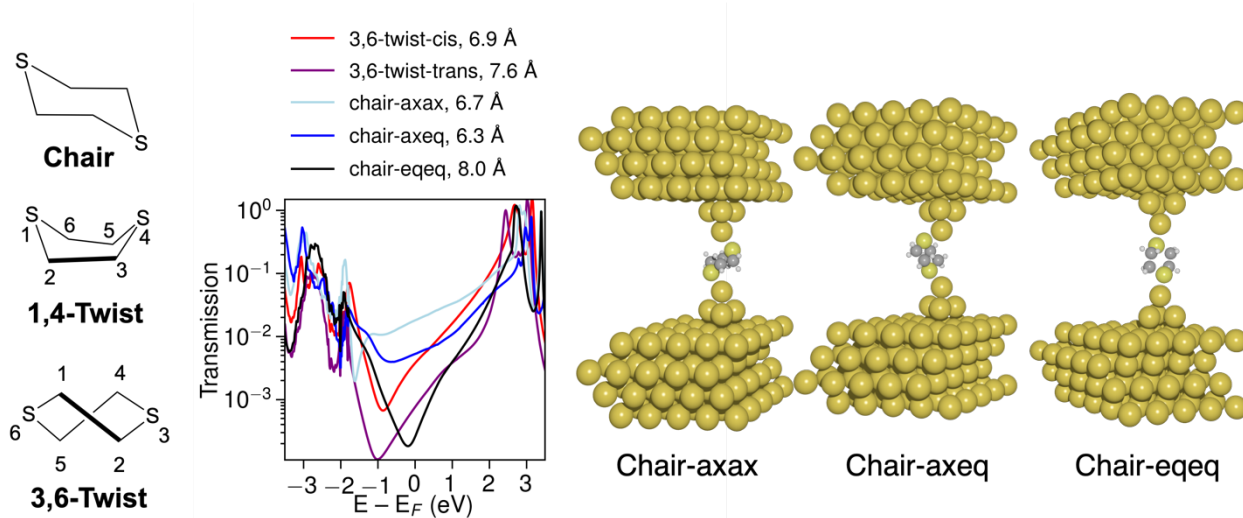


Figure S7. Overview of possible conformations of **dithiane**, and Au-molecule-Au junction transmission with Au-Au tip-to-tip length.

Table S2. Energies of **dithiane** conformations (M06-2X(D3)/6-311G(d,p)).

Conformations (vacuum)	eV
Chair	0.00
36Twist	0.19

4. Computational Details

All electronic structure computations presented were carried out using density functional theory (DFT) as implemented in the Atomic Simulation Environment (ASE) and GPAW.^{5, 6} The molecular structures were optimized to a force threshold of 0.01 eV/Å using DFT with the Perdew-Burke-Ernzerhof (PBE) functional.⁷ We used a double- ζ plus polarization (DZP) basis set for all atoms.⁸ This level of theory was chosen in order to carry out the transport calculations. Molecular structures and current density plots were made using Jmol.⁹ All junction structures are available online in xyz format as supplementary files.

Electron transport calculations were carried out using the non-equilibrium Green's functions (NEGF) approach in combination with DFT as implemented in ASE and GPAW.^{5, 6} The retarded and advanced Green's functions, $G^{r/a}(E)$, are calculated from the Hamiltonian and overlap matrix of the molecular region, H_M and S_M , and the self-energies of the left and right electrodes, $\Sigma_{L/R}^{r/a}(E)$,

$$G^{r/a}(E) = [E \cdot S_M - H_M - \Sigma_L^{r/a}(E) - \Sigma_R^{r/a}(E)]^{-1}. \quad (\text{S1})$$

The Landauer transmission, $T(E)$, is then calculated using the coupling matrices of the left and right electrodes, $\Gamma_{L/R}$,

$$T(E) = \text{tr}[\Gamma_L(E)G^r(E)\Gamma_R(E)G^a(E)]. \quad (\text{S2})$$

As described in the manuscript, Au-molecule-Au junctions are constructed by placing the molecule between two four-atom Au pyramids on 4 x 4 Au(111) surfaces with periodic boundary conditions in the plane of the surfaces. The junction structure is relaxed to a force threshold of 0.05 eV/Å with all Au atoms kept fixed during the optimization. The Landauer transmission $T(E)$ is computed using equation (2) with a k-point sampling over a 4 x 4 x 1 Monkhorst–Pack mesh in the first Brillouin zone.

The current density calculations presented in the manuscript and in Figure S3 are modelled using single-molecule junctions with wide-band limit approximated s-band electrodes. These junctions were formed using two dihydrogen molecules placed with an S-H distance of 1.75 Å or N-H distance of 1.50 Å, thus coupling into the S or N lone-pair (see Figure S4) and forming the extended molecular region used in equation 1. The s-band electrode regions are formed by nonzero matrix elements of $\Gamma_{L/R}$ set to $\gamma = 1.0$ eV. This approach gives a qualitatively similar transmission to using periodic Au-electrodes, and allows us to calculate the ballistic current density.^{10, 11} The transmission and current density calculations using this setup, were carried out using DFT with the PBE functional and DZP basis set for all atoms except hydrogen where a SZ basis was used. We carried out these calculations using our homemade transport and current density code which is compatible with GPAW and ASE,^{5,6} and freely available [online](#).

At zero-temperature and absent of an external magnetic field, the low-bias current density $\mathbf{j}(\mathbf{r})$ can be calculated by equation 3 and 4 using the NEGF formalism. Here, ψ are basis functions, and C are the functions within the extended molecular region which we sum over.^{12, 13}

$$\mathbf{j}(\mathbf{r}) = \frac{ie^2\hbar}{4m\pi} \sum_{i,j \in C} \int_{-\infty}^{\infty} dE G_{ij}^n [\psi_i(\mathbf{r})\nabla\psi_j(\mathbf{r}) - \psi_j(\mathbf{r})\nabla\psi_i(\mathbf{r})] \quad (\text{S3})$$

$$G^n = iG^r\Gamma_L G^a\delta V \quad (\text{S4})$$

In equation 4, G^n is the non-equilibrium part of the lesser Green's function and δV is a small symmetric bias difference between the electrodes, which we set to $\delta V = 1$ mV. We plot the current density vector field ($\mathbf{j}(\mathbf{r})$) as three dimensional arrows (Figure S4), or as a slice of the vector field along the z-axis, which is the transport direction. The magnitude of the current density is scaled relative to the largest vector (highest current density) in the same figure. Vectors smaller than 2% of the largest z-component (forward current) are not included. We note that ballistic current density calculations can have serious issues with current conservation over the molecule due to using a finite local basis set and approximated core-potentials.^{10, 14-20} In the manuscript, we therefore focus our interpretation on z-slices where the current density converges to the total current. The error associated with the current density can be assessed by integrating $\mathbf{j}(\mathbf{r})$ over a plane, \mathbf{A} , perpendicular to the transport direction, z .

$$J = \int \mathbf{j}(\mathbf{r})d\mathbf{A}, \quad d\mathbf{A} = dx dy \quad (\text{S5})$$

The current through the plane J is directly comparable with the total current, which we denote I , that can be calculated using the general Landauer formula.

$$I = \frac{e\hbar}{2\pi} \int dE (f_L(E) - f_R(E)) \cdot T(E), \quad (\text{S6})$$

where $T(E)$ is the transmission function and $f_{L/R}$ are the fermi functions of the left and right electrodes. Ideally, J should equal I at any chosen surface of integration (**A**) across the transport direction. However, this is rarely the case. In Figure S9, we include the current as a function of the z -coordinate (the transport direction) for the junctions shown in Figure S5. It is important to note, that there are parts of the molecule where the current is not perfectly conserved. Thus, the current density vector fields shown in Figure 3 and Figure S5 should only be interpreted qualitatively. Still we note that the current density is almost fully converged in the central part of **C222-diaza**, where strong through-space current appears. This is also in general the case for other molecules, and convergence issues seem to be happening mainly at the N and S atoms where injection occurs.

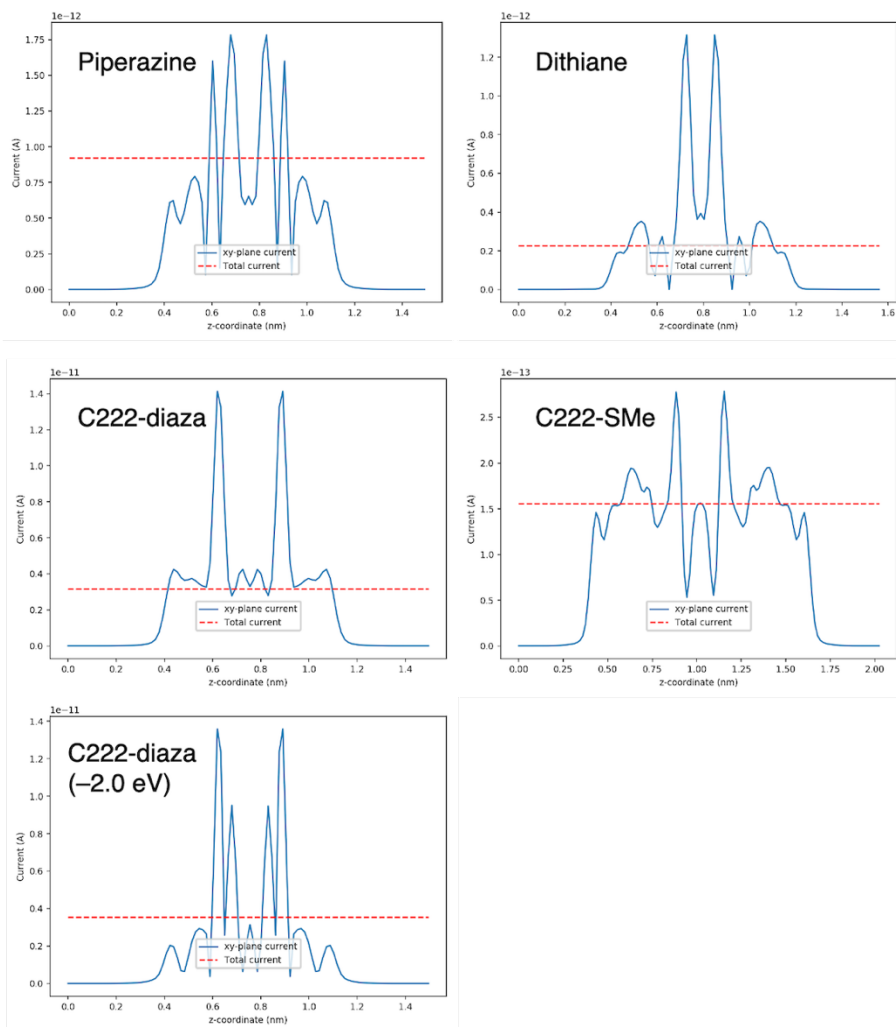


Figure S8. Current calculated with 1.0 meV bias around the Fermi energy (except where otherwise noted) using equation S5 (blue) and S6(red) for **piperazine**, **C222-diaza**, **dithiane**, and **C222-SMe** at the during torsion.

5. References:

- (1) Venkataraman, L.; Klare, J. E.; Nuckolls, C.; Hybertsen, M. S.; Steigerwald, M. L. *Nature* **2006**, 442, (7105), 904-907.
- (2) Garner, M. H.; Li, H.; Neupane, M.; Zou, Q.; Liu, T.; Su, T. A.; Shangguan, Z.; Paley, D. W.; Ng, F.; Xiao, S.; Nuckolls, C.; Venkataraman, L.; Solomon, G. C. *J. Am. Chem. Soc.* **2019**, 141, (39), 15471-15476.
- (3) Frisch, M. J.; Trucks, G. W.; Schlegel, H. B.; G. E. Scuseria; Robb, M. A.; Cheeseman, J. R.; Scalmani, G.; Barone, V.; B. Mennucci; Petersson, G. A.; Nakatsuji, H.; Caricato, M.; Li, X.; Hratchian, H. P.; Izmaylov, A. F.; Bloino, J.; Zheng, G.; Sonnenberg, J. L.; Hada, M.; Ehara, M.; Toyota, K.; Fukuda, R.; Hasegawa, J.; Ishida, M.; Nakajima, T.; Honda, Y.; Kitao, O.; Nakai, H.; Vreven, T.; J. A. Montgomery, J.; Peralta, J. E.; Ogliaro, F.; Bearpark, M.; Heyd, J. J.; Brothers, E.; Kudin, K. N.; Staroverov, V. N.; Keith, T.; Kobayashi, R.; Normand, J.; Raghavachari, K.; Rendell, A.; Burant, C.; Iyengar, S. S.; Tomasi, J.; Cossi, M.; Rega, N.; Millam, J. M.; Klene, M.; Knox, J. E.; Cross, J. B.; Bakken, V.; Adamo, C.; Jaramillo, J.; Gomperts, R.; Stratmann, R. E.; Yazyev, O.; Austin, A. J.; Cammi, R.; Pomelli, C.; Ochterski, J. W.; Martin, R. L.; Morokuma, K.; Zakrzewski, V. G.; Voth, G. A.; Salvador, P.; Dannenberg, J. J.; Dapprich, S.; Daniels, A. D.; Farkas, O.; Foresman, J. B.; Ortiz, J. V.; Cioslowski, J.; Fox, D. J. *Gaussian 09, Rev. D.01*, Gaussian, Inc., Wallingford CT, 2013.: 2013.
- (4) Zhao, Y.; Truhlar, D. G. *Theor. Chem. Acc.* **2008**, 120, (1), 215-241.
- (5) Enkovaara, J.; Rostgaard, C.; Mortensen, J. J.; Chen, J.; Dułak, M.; Ferrighi, L.; Gavnholt, J.; Glinsvad, C.; Haikola, V.; Hansen, H. A.; Kristoffersen, H. H.; Kuisma, M.; Larsen, A. H.; Lehtovaara, L.; Ljungberg, M.; Lopez-Acevedo, O.; Moses, P. G.; Ojanen, J.; Olsen, T.; Petzold, V.; Romero, N. A.; Stausholm-Møller, J.; Strange, M.; Tritsarlis, G. A.; Vanin, M.; Walter, M.; Hammer, B.; Häkkinen, H.; Madsen, G. K. H.; Nieminen, R. M.; Nørskov, J. K.; Puska, M.; Rantala, T. T.; Schiøtz, J.; Thygesen, K. S.; Jacobsen, K. W. *J. Phys. Condens. Matter* **2010**, 22, (25), 253202.
- (6) Larsen, A. H.; Mortensen, J. J.; Blomqvist, J.; Castelli, I. E.; Christensen, R.; Dułak, M.; Friis, J.; Groves, M. N.; Hammer, B.; Hargus, C.; Hermes, E. D.; Jennings, P. C.; Jensen, P. B.; Kermode, J.; Kitchin, J. R.; Kolsbjerg, E. L.; Kubal, J.; Kaasbjerg, K.; Lysgaard, S.; Maronsson, J. B.; Maxson, T.; Olsen, T.; Pastewka, L.; Peterson, A.; Rostgaard, C.; Schiøtz, J.; Schütt, O.; Strange, M.; Thygesen, K. S.; Vegge, T.; Vilhelmsen, L.; Walter, M.; Zeng, Z.; Jacobsen, K. W. *J. Phys.: Condens. Matter* **2017**, 29, (27), 273002.
- (7) Perdew, J. P.; Burke, K.; Ernzerhof, M. *Phys. Rev. Lett.* **1996**, 77, (18), 3865-3868.
- (8) Larsen, A. H.; Vanin, M.; Mortensen, J. J.; Thygesen, K. S.; Jacobsen, K. W. *Phys. Rev. B* **2009**, 80, (19), 195112.
- (9) Jmol: an open-source Java viewer for chemical structures in 3D. <http://www.jmol.org/>
- (10) Jensen, A.; Garner, M. H.; Solomon, G. C. *J. Phys. Chem. C* **2019**, 123, (19), 12042-12051.
- (11) Garner, M. H.; Koerstz, M.; Jensen, J. H.; Solomon, G. C. *J. Phys. Chem. Lett.* **2018**, 9, (24), 6941-6947.
- (12) Datta, S., *Electronic Transport in Mesoscopic Systems*. Cambridge University Press: 1995.
- (13) Xue, Y.; Ratner, M. A. *Phys. Rev. B* **2004**, 70, (8), 081404.
- (14) Garner, M. H.; Jensen, A.; Hyllested, L. O. H.; Solomon, G. C. *Chem. Sci.* **2019**, 10, (17), 4598-4608.
- (15) Zhang, L.; Wang, B.; Wang, J. *Phys. Rev. B* **2011**, 84, (11), 115412.
- (16) Cabra, G.; Jensen, A.; Galperin, M. *J. Chem. Phys.* **2018**, 148, (20), 204103.

- (17) Pohl, V.; Marsoner Steinkasserer, L. E.; Tremblay, J. C. *J. Phys. Chem. Lett.* **2019**, 5387-5394.
- (18) Lai, L. Q.; Chen, J.; Liu, Q. H.; Yu, Y. B. *Phys. Rev. B* **2019**, 100, (12), 125437.
- (19) Garner, M. H.; Bro-Jørgensen, W.; Solomon, G. C. *J. Phys. Chem. C* **2020**, 124, (35), 18968–18982.
- (20) Garner, M. H.; Solomon, G. C. *J. Phys. Chem. Lett.* **2020**, 11, (17), 7400-7406.